Chromosome Organization by a Nucleoid-Associated Protein in Live Bacteria

Wenqin Wang, *et al.*

Science **333**, 1445 (2011);
DOI: 10.1126/science.1204697

15. P. Donoso, G. Sanchez, R. Bull, C. Hidalgo, *Front. Biosci.* **16**, 553 (2011).
16. A. Akki, M. Zhang, C. Murdoch, A. Brewer, A. M. Shah, *J. Mol. Cell. Cardiol.* **47**, 15 (2009).
17. C. Jung, A. S. Martins, E. Niggli, N. Shirokova, *Cardiovasc. Res.* **77**, 766 (2008).
18. C. E. Murdoch, M. Zhang, A. C. Cave, A. M. Shah, *Cardiovasc. Res.* **71**, 208 (2006).
19. C. Hidalgo, G. Sánchez, G. Barrientos, P. Aracena-Parks, *J. Biol. Chem.* **281**, 26473 (2006).
20. Y. Li, M. A. Trush, *Biochem. Biophys. Res. Commun.* **253**, 295 (1998).
21. J. A. Byrne *et al.*, *Circ. Res.* **93**, 802 (2003).
22. K. D. Martyn, L. M. Frederick, K. von Loehneysen, M. C. Dinauer, U. G. Knaus, *Cell. Signal.* **18**, 69 (2006).
23. F. E. Rey, M. E. Cifuentes, A. Kiarash, M. T. Quinn, P. J. Pagano, *Circ. Res.* **89**, 408 (2001).
24. A. Best, S. Ahmed, R. Kozma, L. Lim, *J. Biol. Chem.* **271**, 3756 (1996).
25. G. Sánchez *et al.*, *Cardiovasc. Res.* **77**, 380 (2008).
26. L. F. Santana, H. Cheng, A. M. Gómez, M. B. Cannell, W. J. Lederer, *Circ. Res.* **78**, 166 (1996).
27. I. A. Williams, D. G. Allen, *Am. J. Physiol. Heart Circ. Physiol.* **292**, H846 (2007).
28. S. Hein, S. Kostin, A. Heling, Y. Maeno, J. Schaper, *Cardiovasc. Res.* **45**, 273 (2000).

Acknowledgments: We thank S. Martin for antibodies to tubulin subunits and for discussion, G. Shi for technical assistance, and M. Williams for NOX2$^{-/-}$ animals. B.L.P is supported by an NIH training grant (T32 HL072751-07) to the Training Program in Cardiovascular Cell Biology. This work was supported by NIH grants R01 HL106059, P01 HL67849, R01 HL36974, RC2 NR011968, and S10 RR023028; Leducq North American-European Atrial Fibrillation Research Alliance; European Union Seventh Framework Program (FP7), Georg August University, "Identification and therapeutic targeting of common arrhythmia trigger mechanisms"; and the Maryland Stem Cell Research Fund. World Precision Instruments (WPI, Sarasota, FL, USA and SI-Heidelberg), Gabe Sinclair (Fourhourday, Baltimore, MD, USA), and Siskiyou (Grants Pass, OR, USA) supported instrumentation and equipment development.

Supporting Online Material
www.sciencemag.org/cgi/content/full/333/6048/1440/DC1
Materials and Methods
Figs. S1 to S11
References (*29*–*31*)
Movies S1 and S2

11 January 2011; accepted 18 July 2011
10.1126/science.1202768

Chromosome Organization by a Nucleoid-Associated Protein in Live Bacteria

Wenqin Wang,[1]* Gene-Wei Li,[1,2]* Chongyi Chen,[2,3]* X. Sunney Xie,[2]† Xiaowei Zhuang[1,2,4]†

Bacterial chromosomes are confined in submicrometer-sized nucleoids. Chromosome organization is facilitated by nucleoid-associated proteins (NAPs), but the mechanisms of action remain elusive. In this work, we used super-resolution fluorescence microscopy, in combination with a chromosome-conformation capture assay, to study the distributions of major NAPs in live *Escherichia coli* cells. Four NAPs—HU, Fis, IHF, and StpA—were largely scattered throughout the nucleoid. In contrast, H-NS, a global transcriptional silencer, formed two compact clusters per chromosome, driven by oligomerization of DNA-bound H-NS through interactions mediated by the amino-terminal domain of the protein. H-NS sequestered the regulated operons into these clusters and juxtaposed numerous DNA segments broadly distributed throughout the chromosome. Deleting H-NS led to substantial chromosome reorganization. These observations demonstrate that H-NS plays a key role in global chromosome organization in bacteria.

The structure of the bacterial chromosome and the molecular mechanisms underlying its organization are poorly understood, in part due to the lack of appropriate tools for visualizing the chromosome in vivo. Fluorescence microscopy experiments have shown that DNA occupies only the central part of the bacterial cell, referred to as the nucleoid (*1*), but the diffraction-limited optical resolution prevents a detailed characterization. Ultrastructural characterization of the nucleoid by electron microscopy has provided varying results depending on the procedures used to fix, dehydrate, and embed the cells (*1*, *2*). Recently, labeling of specific gene loci with the use of fluorescence in situ hybridization and fluorescent repressor-operator systems has allowed imaging of individual gene positions, and their relationship to DNA replication and segregation, in fixed and live bacterial cells (*3*–*5*). However, these studies probe only one set of specific loci at a time, and the global chromosome organization remains unclear.

In bacteria, major nucleoid-associated proteins (NAPs) are the most abundant factors that associate with the chromosome (*6*, *7*). In *Escherichia coli*, major NAPs include H-NS, HU, Fis, IHF, and StpA (*6*). Each of these NAPs binds up to hundreds of specific sites per chromosome (*6*, *8*, *9*). Moreover, because of their substantial nonspecific DNA-binding affinity, the majority of cellular NAPs are bound to the chromosomal DNA with a coverage of roughly one NAP per 100 base pairs of DNA (*10*). NAPs have two major functions: gene regulation and chromosome organization (*7*). In particular, H-NS preferentially binds to AT-rich sequences (*8*, *9*, *11*–*13*), functions as a global transcriptional silencer of genes with high AT content (*14*, *15*), and is thought to reside at the center of the nucleoid (*16*). The oligomerization of H-NS can promote higher-order DNA structures in vitro (*17*), potentially through DNA looping, bridging, and/or stiffening (*18*–*20*). These biophysical properties of NAPs and their numerous binding sites on DNA have led to the hypothesis that NAPs potentially act as chromosome organizing centers (*21*). However, whether the implicated higher-order DNA structures induced by NAPs exist in vivo and how the chromosome is globally organized by the NAPs remain unknown.

In a live bacterial cell, a single protein, upon binding to the less mobile structures such as the cell membrane or chromosome, can be detected and localized against a strong cellular autofluorescence background (*22*–*24*). However, the diffraction-limited optical resolution limits this imaging approach to proteins with low copy numbers in the cell (*24*). To obtain the subcellular distribution and organization of the abundant bacterial NAPs, sub–diffraction-limit image resolution is required.

Here, we used localization-based super-resolution imaging [stochastic optical reconstruction microscopy (STORM) or photoactivated localization microscopy] (*25*–*29*) to survey the subcellular distributions of major NAPs: H-NS, HU, Fis, IHF, and StpA. Unless otherwise specified, we tagged the target of interest with a monomeric photoactivatable fluorescent protein, mEos2 (*30*). We then created *E. coli* strains in which the fusion proteins were expressed from their native promoters at the endogenous loci, allowing the targets to be fully labeled and expressed approximately at the wild-type (WT) level (table S1) (*31*). All of these mEos2 fusion strains exhibited the same growth rates (cell-doubling times) as the wild type (*31*). Cells were imaged in a M9 minimal medium supplemented with glucose at room temperature shortly after they were removed from the 37°C culture at the early log phase (*31*).

To acquire a super-resolution image, we used a weak 405-nm light to activate the mEos2 molecules such that only an optically resolvable subset of molecules were activated at any given instant. We then illuminated the activated molecules with a 561-nm light and used astigmatism imaging to determine their centroid positions in all three dimensions, as previously shown in three-dimensional (3D) STORM (*32*). The molecular localizations accumulated over time allowed a

[1]Department of Physics, Harvard University, Cambridge, MA 02138, USA. [2]Department of Chemistry and Chemical Biology, Harvard University, Cambridge, MA 02138, USA. [3]Department of Molecular and Cellular Biology, Harvard University, Cambridge, MA 02138, USA. [4]Howard Hughes Medical Institute, Harvard University, Cambridge, MA 02138, USA.

*These authors contributed equally to the work.
†To whom correspondence should be addressed. E-mail: xie@chemistry.harvard.edu (X.S.X.); zhuang@chemistry.harvard.edu (X.Z.)

sub–diffraction-limit image to be constructed. We used a continuous activation and imaging mode (*33*), allowing ~1000 molecules per cell to be imaged every minute. Only a subset of the mEos2 label could mature and become fluorescent due to the long maturation time of mEos2 compared with the *E. coli* doubling time (*30*). Among those that matured, only a subset could be activated by the 405-nm light. The laser illumination used for imaging did not exert an appreciable effect on cell viability, as evident from the nearly identical (within 10%) cell-doubling times observed with or without illuminations.

Notably, H-NS formed a few compact clusters within each cell (Fig. 1A and movie S1). The majority of H-NS molecules resided in these clusters, whose fluorescence accounted for 60 ± 25% of the total activated mEos2 signal (*31*). To test the functional integrity of the mEos2-tagged H-NS, we measured the expression levels of *hdeA* and *hchA*, two genes repressed by H-NS (*15*). The strain expressing the fluorescent fusion protein retained WT activity in repressing these two genes (fig. S1) (*31*). As a control, the expression levels of *lacZ*, a gene not regulated by H-NS, were similar in the WT, fluorescent-fusion, and H-NS–deletion strains (fig. S1).

In contrast to the clustered distribution of H-NS, HU was largely scattered throughout the nucleoid (Fig. 1B), consistent with recent data from another bacterial species, *Caulobacter crescentus* (*34*). We observed similar distributions for Fis and IHF, albeit at lower expression levels (fig. S2) (*31*). StpA also displayed a scattered distribution in the nucleoid (fig. S2), despite being a paralog of H-NS (*14*). Interestingly, Rok, a *Bacillus subtilis* protein functionally analogous to H-NS but lacking any sequence homology, is distributed nonuniformly in the nucleoid (*35*). In addition to the NAPs, we also imaged the ribosomes, which should be excluded from the nucleoid (*1*). As expected, the ribosomes were enriched in the cell periphery (fig. S3) (*31*).

Next, we examined the molecular mechanisms responsible for the formation of H-NS clusters in vivo. H-NS has two structural domains: (i) an N-terminal domain that promotes dimerization and oligomerization and (ii) a C-terminal domain

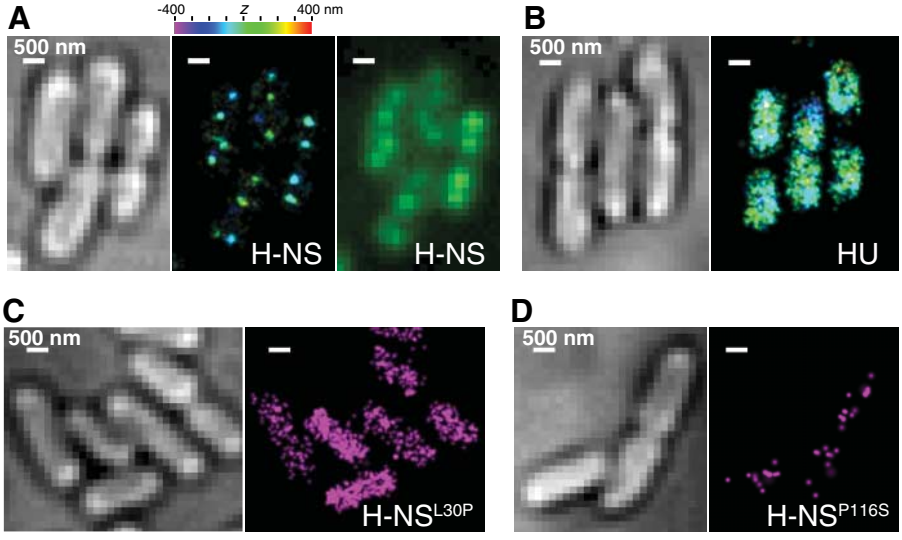

Fig. 1. Super-resolution imaging of major nucleoid-associated proteins in living *E. coli* cells. (**A**) Compact H-NS clusters in the nucleoid. The *E. coli* cells shown in the bright-field image (left) expressed photoactivatable fluorescent protein mEos2 fused to H-NS, which was imaged with sub–diffraction-limit resolution (middle). The *z* coordinate of each localization in the 3D STORM image is color-coded according to the color bar (top). In comparison, a conventional fluorescence image of the same cells is shown (right). A time-lapse movie corresponding to the super-resolution image is available as movie S1 (*31*). Due to the slow cluster movements, the images of H-NS are not motion-blurred appreciably. (**B**) Scattered distribution of HU in the nucleoid. (Left) Bright-field image; (right) 3D STORM image of mEos2-labeled HU in the same cells. Similar distributions were observed for Fis, IHF, and StpA (fig. S2) (*31*). Fine features of the nucleoid shape could potentially be blurred by movement. (**C** and **D**) Dependence of H-NS cluster formation on its oligomerization and DNA-binding capabilities. (C) Bright-field image of cells (left) and corresponding 2D super-resolution image of H-NS (right) with a point mutation, L30P, that inhibits dimerization/oligomerization. (D) Bright-field image (left) and corresponding 2D super-resolution image of H-NS (right) with a point mutation, P116S, that inhibits DNA binding. Image acquisition time: 0.5 to 2 min for each image.

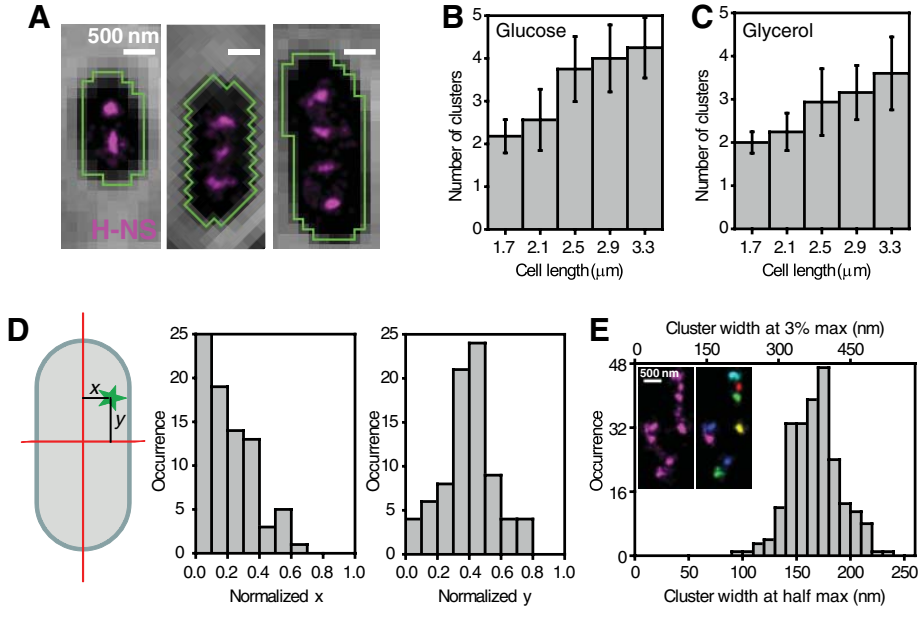

Fig. 2. Quantitative characterizations of the H-NS clusters. (**A** to **C**) Number of clusters per cell. (A) Overlay of the phase contrast images showing the cell contours (segmentation shown in green) and the super-resolution images of H-NS (magenta) for three cells of different lengths. (B and C) Average number of clusters per cell versus the cell length is shown for different growth conditions [medium supplemented with glucose (B) or glycerol (C)]. Error bars indicate SD [n = 28, 32, 32, 14, and 4 cells from left to right for (B) and n = 34, 49, 31, 32, and 10 cells from left to right for (C)]. (**D**) Location of the clusters. Each cluster (green) was assigned a coordinate (x, y) relative to the cell axes (left). (Right) For cells with two clusters, the distributions of cluster coordinates are plotted for x normalized to the half cell width and y normalized to the half cell length. For cells with three clusters, the (x, y) distributions are shown in fig. S5 (*31*). (**E**) Size of the clusters. The distribution of the FWHM (bottom axis) or full width at 3% maximum (top axis) of the clusters was determined with automated cluster identification [example image (left) and segmentation (right) shown in inset] (*31*). Image acquisition time: 1 min.

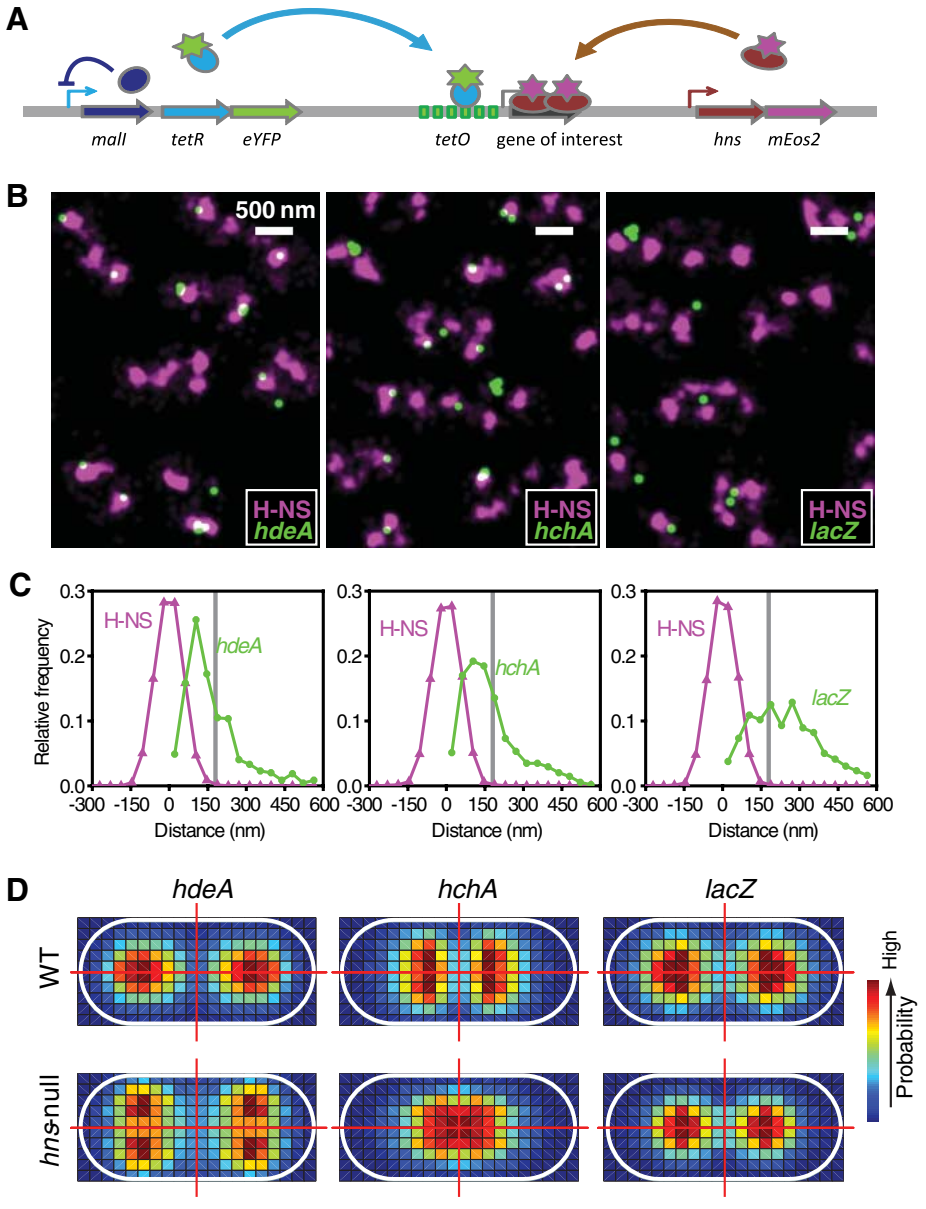

Fig. 3. Colocalization of H-NS clusters and specific gene loci. (**A**) Two-color imaging scheme of mEos2-labeled H-NS and eYFP-labeled gene locus as described in the text. (**B**) Two-color live-cell images of H-NS (magenta) and the *hdeA*, *hchA*, or *lacZ* loci (green), showing more extensive H-NS colocalization for *hdeA* and *hchA*. Because each blinking event of eYFP was imaged independently, a single gene locus may appear as more than one puncta. (**C**) Quantitative colocalization analysis between H-NS clusters and the *hdeA*, *hchA*, or *lacZ* loci. Green curves, 2D-distance distributions between the gene loci and the center positions of their nearest H-NS clusters; magenta curves, density cross sections of these H-NS clusters aligned to their center positions. Approximately 67% of *hdeA*, 65% of *hchA*, and 36% of *lacZ* loci resided within the boundary of the clusters (defined by the gray vertical lines, positioned at 3% of the peak values of the magenta curves) (*31*). The 3% line was chosen as the cluster boundary because the background density outside the clusters was only ~1% of the peak densities. The colocalization fraction of *lacZ* is close to the expected background value (20 to 30%), derived from a random distribution of the gene locus in the nucleoid. To remove the potential artifact due to cluster-size heterogeneity associated with this ensemble analysis, we performed an alternative single-locus–based analysis, which also showed that *hdeA* and *hchA* colocalized with H-NS clusters to a substantially higher degree than *lacZ* (*31*). In each case, 500 to 700 gene locus positions were analyzed. (**D**) Displacement of gene loci upon H-NS deletion. The 2D histograms of the relative *hdeA*, *hchA*, and *lacZ* locus positions normalized to the cell dimensions are shown. Considering the approximate mirror symmetry of the cell shape along its long and short axes observed in the bright-field images, we placed normalized locus positions into the first quartile of the cell and then extended the probability density map into the other three quartiles by enforcing the mirror symmetry. Therefore, symmetric peaks within the cell do not necessarily reflect the presence of more than one most probable position of the gene locus. The grid size is ~100 to 200 nm, and the probability density is color-coded according to the color bar (right). White ovals, cells outlines; red lines, cell axes. In each case, 2000 to 5000 gene locus positions were analyzed.

that binds to DNA (*17*–*19*). We tested the effects of these functions on the cluster formation by introducing an N-terminal point mutation $Leu^{30}\rightarrow Pro^{30}$ (L30P) that inhibits H-NS dimerization (*36*) or a C-terminal point mutation $Pro^{116}\rightarrow Ser^{116}$ (P116S) that inhibits DNA binding (*37*, *38*) into the chromosomally expressed H-NS–mEos2 fusion protein. The expression levels of the two mutants were comparable to that of the wild type (table S1) (*31*). Both mutations abolished the silencing effect of H-NS on *hdeA* and *hchA*, but had little influence on *lacZ* expression (fig. S1). In contrast to the WT H-NS, $H\text{-}NS^{L30P}$ did not form clusters, but was scattered throughout the nucleoid (Fig. 1C), indicating that cluster formation was induced by the N-terminal domain–driven oligomerization of the protein. In the cells expressing $H\text{-}NS^{P116S}$, the number of observed localizations was reduced by ~20-fold compared with the H-NS–expressing cells (Fig. 1D), indicating that the localizations of H-NS were primarily due to molecules bound to DNA.

To quantify the effect of H-NS clustering on chromosome organization, we first characterized the number of H-NS clusters per chromosome, as well as the physical location and size of these clusters. Given the cylindrical symmetry of the cells and that the H-NS clusters were rarely observed to line up with each other in the *z* direction, we used 2D projection images for the following quantitative characterizations to take advantage of the superior resolution in the *xy* plane [measured to be ~35 nm in full width at half maximum (FWHM)] compared with that along the *z* direction (~75 nm, FWHM) (*31*).

Most newly divided cells had approximately two clusters, and the number increased with the cell length (Fig. 2, A and B). For the longest cells before division, the cluster number reached four, on average (Fig. 2B). These data suggest an increase in the number of H-NS clusters with the chromosome copy number. To test whether the specific fluorescent protein tag mEos2 had influenced the cluster formation, we fused H-NS with a different monomeric photoactivatable fluorescent protein, PAmCherry1 (*39*). We observed similar clustering for PAmCherry1-labeled H-NS (fig. S4). Subsequent analyses of H-NS clusters were performed on mEos2-labeled samples.

To determine the number of clusters per chromosome, we reduced the cell growth rate by using a glycerol-supplemented minimal medium to ensure that each newly divided cell had exactly one copy of the chromosome (*31*). Under this condition, we observed two H-NS clusters in the shortest cells (Fig. 2C), suggesting that there are ~two H-NS clusters associated with each copy of the chromosome. These two clusters were preferentially located near the one-quarter and three-quarter positions along the long axis of the cell (Fig. 2D). In cells that had three clusters, the additional cluster tended to appear in the middle (fig. S5) (*31*).

To characterize the cluster size, we determined the localization distributions within the

clusters. The widths of the distributions were, on average, ~160 nm measured at half-maximum density and ~360 nm at 3% of the maximum (Fig. 2E). The background localization density outside the clusters was only ~1% of the peak densities in the clusters. The cluster size was substantially larger than both our localization precision (~35 nm) and the cluster movement during the observation time (~40 to 50 nm over 0.5 to 2 min). Moreover, the measured cluster size did not change appreciably when we changed the imaging time from 0.5 to 1 min. These results indicate that neither localization precision nor motion blurring had substantial effects on our measurements on the H-NS clusters.

The above quantifications indicate that the volume occupied by the H-NS clusters in each cell represents only a small fraction of the total nucleoid volume that was estimated to be ~0.2 μm^3 from the volume occupied by HU molecules as well as from previous experiments (*40*). Given that H-NS binding sites are broadly distributed throughout the *E. coli* genome (*8*, *9*), collapsing of the DNA-bound H-NS into two compact clusters must therefore lead to substantial folding of DNA and reorganization of the chromosome on the global scale.

To probe whether the cluster organization of H-NS correlates with its regulatory role, we studied the spatial relationship between H-NS clusters and H-NS–regulated genes. The positions of the gene loci were determined by imaging enhanced yellow fluorescent protein–labeled Tet repressor (TetR-eYFP) bound to *tet* operator (*tetO*) sequences inserted upstream of the genes of interest (Fig. 3A). Unlike previously used fluorescent repressor-operator systems, which typically contain tens to hundreds of tandem repeats of repressor binding sites, we inserted only six *tetO* repeats (219 base pairs) immediately upstream of the target genes to more precisely mark their positions. Using a negative feedback loop regulated by MalI (Fig. 3A) (*41*), we achieved a low expression level of TetR-eYFP that allowed the clear detection of the *tetO*-bound TetR-eYFP above the background (Fig. 3B), though not all target loci were necessarily bound by TetR-eYFP due to the small number of *tetO* sites and the low expression level of TetR-eYFP. These strains had the same growth rates as the wild type (*31*), whereas the strains with a large number of inserted repressor binding sites tend to exhibit growth defects.

The two-color super-resolution images of mEos2-labeled H-NS and eYFP-labeled gene loci were taken using a sequential imaging approach to avoid the spectral cross-talk between eYFP and the preactivation form of mEos2: The mEos2 molecules were first activated using a 405-nm laser and imaged with a 561-nm laser; after all mEos2 molecules were photobleached, the eYFP molecules were imaged using a 514-nm laser. The negligible displacement of the H-NS clusters (~20 nm) during the time taken for eYFP imaging allowed the colocalization between the gene loci and H-NS clusters to be probed in live cells.

Using this approach, we imaged H-NS together with the loci of *hdeA*, *hchA*, and *lacZ* genes, the former two of which are regulated by H-NS (fig. S1). As shown in Fig. 3, B and C, *hdeA* and *hchA* colocalized with H-NS clusters to a substantially larger extent than did *lacZ*, indicating that the H-NS–regulated operons are preferentially sequestered into the H-NS clusters. Interestingly, whereas the H-NS clusters themselves appeared largely static, both *hdeA* and *hchA* loci were mobile and did not always colocalize with the clusters, suggesting that the nucleoprotein complex is a heterogeneous and dynamic entity.

By sequestering the regulated genes, the H-NS clusters could potentially cause a substantial reorganization of the chromosome. To test this effect, we probed the positions of *hdeA*, *hchA*, and *lacZ* in the WT versus *hns*-null strains. We determined the position of the labeled gene locus relative to the cell's long and short axes; Fig. 3D shows the probability density maps of these gene loci obtained from many cells. Notably, the positions of *hdeA* and *hchA* loci in *hns*-null cells were both shifted by ~300 nm compared with the WT cells, a distance comparable to the radius of the nucleoid. In contrast, the position of the *lacZ* gene remained largely unchanged (shifted less than 60 nm) upon *hns* deletion.

To further test the long-range chromosome interactions induced by H-NS clustering, we per-

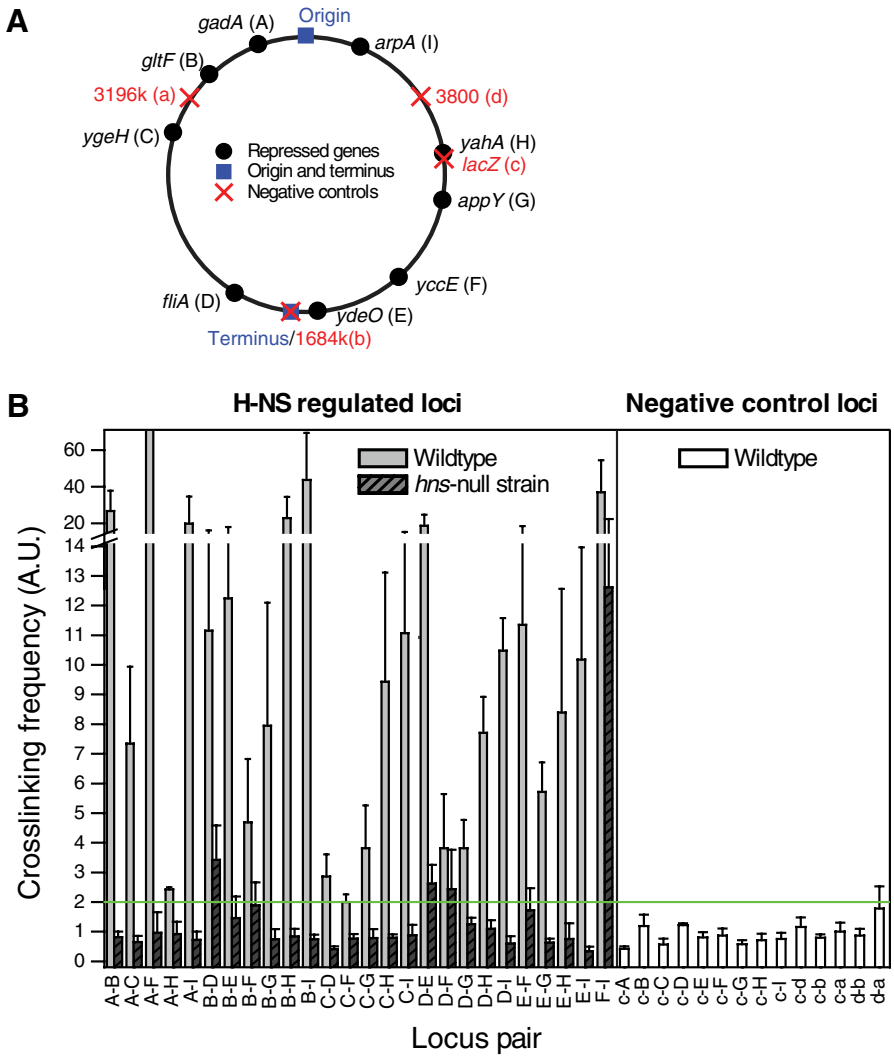

Fig. 4. Proximity between gene locus pairs probed by chromosome conformation capture (3C). (**A**) Nine H-NS–regulated gene loci (labeled as "A" to "I," black circles) and four negative control loci (labeled as "a" to "d," red crosses) on the circular *E. coli* chromosome map. The origin and terminus of replication are marked with blue squares as position references. (**B**) Cross-linking frequencies between pairs of chromosome loci. The cross-linking efficiency is defined as the ratio of qPCR signals between the cross-linked sample and the non–cross-linked control. Each column represents one pair of H-NS–regulated loci (gray bars) or one pair involving at least one negative control loci (white bars). The cross-linking frequencies of the *hns*-null cells are shown for the regulated pairs in dark gray, hatched bars. The horizontal green line marks a twofold difference between cross-linked and non–cross-linked cells. These data reflect the population average behavior, and the proximity pattern between the gene locus pairs could vary from cell to cell. Error bars indicate SEM (n = 3 sets of independent experiments). A.U., arbitrary units.

formed a chromosome conformation capture (3C) assay (*42*) to probe the spatial proximity among various H-NS–regulated genes. In this assay, DNA segments brought into proximity by protein-mediated interactions were captured by formaldehyde cross-linking, followed by restriction enzyme digestion. The cross-linked DNA segments were then ligated and probed by quantitative polymerase chain reaction (qPCR) with specifically designed primer pairs. The amount of PCR products relative to those obtained from non–cross-linked cells should scale with the cross-linking frequency, which in turn reflects the relative proximity between the DNA segments.

Using this approach, we tested the pairwise proximity among nine H-NS–regulated genes broadly distributed along the *E. coli* genome (Fig. 4A), which gave a total of 36 possible pairs. In addition, we selected three random loci on the genome plus *lacZ* as four negative control sites (Fig. 4A). The six pairs among these four sites and the nine pairs between *lacZ* and each of the nine H-NS–regulated genes constituted a total of 15 control pairs. Out of the 36 pairs of H-NS–regulated gene loci, 10 showed PCR priming errors, whereas the remaining 26 pairs gave quantifiable results. Likewise, 14 out of 15 control pairs gave quantifiable results. Because all control pairs showed cross-linking frequencies less than two (Fig. 4B, right), we designated two as the background value. The vast majority of the H-NS–regulated locus pairs (25 out of 26 pairs) yielded cross-linking frequency values larger than the background level, all of which showed reduced cross-linking frequency values upon *hns* deletion, suggesting protein-induced juxtaposition of these loci (Fig. 4B, left). Taken together, these results indicate that the H-NS clusters bring many gene loci into proximity and thus mediate long-range interactions in the chromosome.

Overall, our results demonstrate that H-NS forms a few compact clusters in the chromosome, with cluster formation driven by oligomerization of H-NS bound to DNA. The genes regulated by H-NS are specifically sequestered into these clusters. Given that H-NS is a global transcriptional silencer that regulates ~5% of all *E. coli* genes (*43*) and binds to many DNA sites broadly distributed along the *E. coli* genome (*8*, *9*, *11*–*13*), the cluster formation of H-NS and, consequently, the juxtaposition of DNA segments interacting with H-NS must cause substantial folding and condensation of the bacterial DNA. The H-NS clusters could thus serve as anchoring points for numerous DNA loci distributed throughout the genome, potentially creating DNA loops connecting the anchored loci. These anchor points (or organizing centers) can act in concert with the previously described chromosome domains (*4*, *5*) to shape the 3D architecture of the *E. coli* chromosome.

References and Notes

1. C. Robinow, E. Kellenberger, *Microbiol. Rev.* **58**, 211 (1994).
2. M. Eltsov, B. Zuber, *J. Struct. Biol.* **156**, 246 (2006).
3. Z. Gitai, M. Thanbichler, L. Shapiro, *Trends Microbiol.* **13**, 221 (2005).
4. R. Reyes-Lamothe, X. Wang, D. Sherratt, *Trends Microbiol.* **16**, 238 (2008).
5. O. Espéli, F. Boccard, *J. Struct. Biol.* **156**, 304 (2006).
6. R. C. Johnson, L. M. Johnson, J. W. Schmidt, J. F. Gardner, in *The Bacterial Chromosome*, N. P. Higgins, Ed. (ASM Press, Washington, DC, 2005), chap. 1.5.
7. S. C. Dillon, C. J. Dorman, *Nat. Rev. Microbiol.* **8**, 185 (2010).
8. D. C. Grainger, D. Hurd, M. D. Goldberg, S. J. Busby, *Nucleic Acids Res.* **34**, 4642 (2006).
9. T. Oshima, S. Ishikawa, K. Kurokawa, H. Aiba, N. Ogasawara, *DNA Res.* **13**, 141 (2006).
10. G.-W. Li, O. G. Berg, J. Elf, *Nat. Phys.* **5**, 294 (2009).
11. W. W. Navarre *et al.*, *Science* **313**, 236 (2006); 10.1126/science.1128794.
12. S. Lucchini *et al.*, *PLoS Pathog.* **2**, e81 (2006).
13. B. Lang *et al.*, *Nucleic Acids Res.* **35**, 6330 (2007).
14. C. J. Dorman, *Nat. Rev. Microbiol.* **2**, 391 (2004).
15. F. C. Fang, S. Rimsky, *Curr. Opin. Microbiol.* **11**, 113 (2008).
16. V. McGovern, N. P. Higgins, R. S. Chiz, A. Jaworski, *Biochimie* **76**, 1019 (1994).
17. C. P. Smyth *et al.*, *Mol. Microbiol.* **36**, 962 (2000).
18. S. Rimsky, *Curr. Opin. Microbiol.* **7**, 109 (2004).
19. R. T. Dame, M. C. Noom, G. J. Wuite, *Nature* **444**, 387 (2006).
20. Y. Liu, H. Chen, L. J. Kenney, J. Yan, *Genes Dev.* **24**, 339 (2010).
21. T. Vora, A. K. Hottes, S. Tavazoie, *Mol. Cell* **35**, 247 (2009).
22. J. Deich, E. M. Judd, H. H. McAdams, W. E. Moerner, *Proc. Natl. Acad. Sci. U.S.A.* **101**, 15921 (2004).
23. J. Elf, G.-W. Li, X. S. Xie, *Science* **316**, 1191 (2007).
24. Y. Taniguchi *et al.*, *Science* **329**, 533 (2010).
25. M. J. Rust, M. Bates, X. Zhuang, *Nat. Methods* **3**, 793 (2006).
26. E. Betzig *et al.*, *Science* **313**, 1642 (2006); 10.1126/science.1127344.
27. S. T. Hess, T. P. Girirajan, M. D. Mason, *Biophys. J.* **91**, 4258 (2006).
28. J. S. Biteen *et al.*, *Nat. Methods* **5**, 947 (2008).
29. B. Huang, H. Babcock, X. Zhuang, *Cell* **143**, 1047 (2010).
30. S. A. McKinney, C. S. Murphy, K. L. Hazelwood, M. W. Davidson, L. L. Looger, *Nat. Methods* **6**, 131 (2009).
31. Materials and methods and other supporting materials are available on *Science* Online.
32. B. Huang, W. Wang, M. Bates, X. Zhuang, *Science* **319**, 810 (2008); 10.1126/science.1153529.
33. A. Egner *et al.*, *Biophys. J.* **93**, 3285 (2007).
34. S. F. Lee, M. A. Thompson, M. A. Schwartz, L. Shapiro, W. E. Moerner, *Biophys. J.* **100**, L31 (2011).
35. W. K. Smits, A. D. Grossman, *PLoS Genet.* **6**, e1001207 (2010).
36. C. Ueguchi, C. Seto, T. Suzuki, T. Mizuno, *J. Mol. Biol.* **274**, 145 (1997).
37. R. Spurio, M. Falconi, A. Brandi, C. L. Pon, C. O. Gualerzi, *EMBO J.* **16**, 1795 (1997).
38. C. Badaut *et al.*, *J. Biol. Chem.* **277**, 41657 (2002).
39. F. V. Subach *et al.*, *Nat. Methods* **6**, 153 (2009).
40. W. Schumann, in *Dynamics of the Bacterial Chromosome* (Wiley-VCH, Weinheim, Germany, 2006), chap. 2.2.
41. J. Reidl, W. Boos, *J. Bacteriol.* **173**, 4862 (1991).
42. J. Dekker, K. Rippe, M. Dekker, N. Kleckner, *Science* **295**, 1306 (2002).
43. F. Hommais *et al.*, *Mol. Microbiol.* **40**, 20 (2001).

Acknowledgments: We thank J. Hinton for providing the antibody to H-NS, J. Kaguni for providing the antibody to HU, M. Umbarger and S. Adhya for 3C protocols and discussions, and B. Huang for help with image analysis algorithm. This work was supported in part by the NIH (grant GM 096450 to X.Z. and X.S.X., and NIH Director's Pioneer Award to X.S.X.). G.-W.L. was a NSF predoctoral fellow. X.Z. is a Howard Hughes Medical Institute Investigator.

Supporting Online Material

www.sciencemag.org/cgi/content/full/333/6048/1445/DC1
Materials and Methods
Figs. S1 to S5
Table S1
References (*44*–*49*)
Movie S1

23 February 2011; accepted 13 July 2011
10.1126/science.1204697

Ribosome Assembly Factors Prevent Premature Translation Initiation by 40*S* Assembly Intermediates

Bethany S. Strunk,[1,6]* Cherisse R. Loucks,[2]* Min Su,[2]* Harish Vashisth,[3,4] Shanshan Cheng,[5] Justin Schilling,[2] Charles L. Brooks III,[3,4,5] Katrin Karbstein,[6]† Georgios Skiniotis[2,4]†

Ribosome assembly in eukaryotes requires approximately 200 essential assembly factors (AFs) and occurs through ordered events that initiate in the nucleolus and culminate in the cytoplasm. Here, we present the electron cryo-microscopy (cryo-EM) structure of a late cytoplasmic 40*S* ribosome assembly intermediate from *Saccharomyces cerevisiae* at 18 angstrom resolution. We obtained cryo-EM reconstructions of preribosomal complexes lacking individual components to define the positions of all seven AFs bound to this intermediate. These late-binding AFs are positioned to prevent each step in the translation initiation pathway. Together, they obstruct the binding sites for initiation factors, prevent the opening of the messenger RNA channel, block 60*S* subunit joining, and disrupt the decoding site. These redundant mechanisms probably ensure that pre-40*S* particles do not enter the translation pathway, which would result in their rapid degradation.

In eukaryotes, the assembly of the ribosomal subunits from the four ribosomal RNAs (rRNAs) (18*S*, 5.8*S*, 25*S*, and 5*S*) and 78 ribosomal proteins is facilitated by a conserved macromolecular machinery comprising ~200 assembly factors (AFs). These proteins, which are mostly essential, catalyze the modification, cleavage from precursor transcripts, and folding of the rRNA and also facilitate the binding of ribosomal proteins (*1*). Although the components of this assembly line have been identified, their functions remain largely unknown. Pioneering electron